Potential mass movements on the Palinuro volcanic chain (southern Tyrrhenian Sea, Italy) and consequent tsunami generation

G. Gallotti [a,*], S. Passaro [b], A. Armigliato [a], F. Zaniboni [a], G. Pagnoni [a], L. Wang [a], M. Sacchi [b], S. Tinti [a], M. Ligi [c], G. Ventura [d,e]

[a] University of Bologna, Department of Physics and Astronomy (DIFA), Bologna, Italy
[b] Institute of Marine Sciences (ISMAR), National Research Council (CNR), Napoli, Italy
[c] Institute of Marine Sciences (ISMAR), National Research Council (CNR), Bologna, Italy
[d] Istituto Nazionale di Geofisica e Vulcanologia (INGV), Roma, Italy
[e] Istituto per lo studio degli impatti Antropici e Sostenibilità in ambiente marino, National Research Council (CNR), Roma, Italy

ARTICLE INFO

ABSTRACT

The Palinuro volcanic chain (PVC) is located about 80 km offshore the Campania region (Italy) in the southern sector of the Tyrrhenian Sea. The chain consists of 15 volcanic edifices aligned in an E-W direction with two distinct major seamounts (Palinuro and Glabro). They cover a 90 km long and 20 km wide area, with a present-day volume of 2700 km^3. Palinuro volcanism emplaced between 0.8 and 0.3 Ma, although shallow seismicity and hydrothermalism indicate an ongoing volcanic activity. A geomorphological analysis of the volcanic chain and data from a multichannel seismic profile reveal large volumes of buried chaotic material suggesting gravity mass sliding from the volcano flanks and slide scars. A stability analysis of the Palinuro flanks has been carried out to determine the sectors potentially prone to sliding in case of shallow volcanic earthquakes. Landslides are simulated by adopting a scenario-based approach. Tsunamis induced by these mass movements and their propagation across the Tyrrhenian Sea are modeled. Results suggest that shallow earthquakes (M ~4.6–4.8) are able to destabilize the flanks of the volcanic chain generating slope failures. Sliding volumes in the order of 1.5 km^3 and 2.4 km^3 may induce waves as high as 1.5 and 6 m, respectively, along the peri-Tyrrhenian coast. Our results underline the need for further investigations on the stability of the submarine volcanoes of the Tyrrhenian basin. These volcanoes are still poorly known although their instability could trigger large tsunamis along the southern Italy coastal sectors. Our recommendation is that multiparametric monitoring networks on PVC and periodic oceanic cruises should be put into action, and further that a systematic evaluation of the tsunami hazard related to possible sliding phenomena on the flanks of the Tyrrhenian seamounts should be performed.

1. Introduction

Several volcanoes display morphological evidences of flank and sector collapses as well as of landslides related to gravity instability processes and volcano dynamics (McGuire, 1996; Voight and Elsworth, 1997; Apuani and Corazzato, 2010; Thouret, 2010). Several factors are responsible for the weakening mechanism of volcanic edifices and consequent flank instability. Endogenous factors include magmatic upraise or withdrawal of shallow reservoirs, hydrothermal processes, volcano-tectonics, and earthquakes, while exogenous factors include rain and, more generally, climatic factors (van Wyk de Vries and Francis, 1997; Reid et al., 2001; van Wyk de Vries and Delcamp, 2016). As for onshore volcanoes, instability of volcanic islands may produce devastating debris-flows, lahars, and landslides, but in addition they and seamounts may trigger tsunamis able to travel hundreds of kilometers in short times (Ward and Day, 2001; Paris, 2015). With respect to tsunamis associated with earthquakes, tsunamis related to volcano instability typically show shorter-period waves, and, with few exceptions (e.g., the 1883 Krakatau tsunami) produce less devastating far-field damages (Okal and Synolakis, 2004; Harbitz et al., 2006). However, their occurrence poses a relevant problem of hazard on the continental coastal zones. On volcanic islands, the more recent tsunami occurred in December 2018 killing 437 people in the Sunda Strait as the result of the explosion and sector collapse of the Anak Krakatoa, Indonesia (Muhari et al., 2019; Putra et al., 2020). In the Tyrrhenian Sea (Italy), the most recent event took place in December 2002 at Stromboli island, and involved the submarine and subaerial sectors of the volcano with a maximum run-up of 8 m along the coast of Stromboli (Maramai et al., 2005). Morphological features of numerous seamounts suggest that partial collapses and submarine landslides occur worldwide. At the Lesser Antilles, Dondin et al. (2016) recognize 52 episodes of sliding in the

* Corresponding author.
E-mail address: glauco.gallotti2@unibo.it (G. Gallotti).

arc and show that at least three flank collapses producing large land-slides have driven the evolution of the Kick-'em-Jenny submarine vol-cano. In 1650, a destructive tsunami was produced by the eruption of the Kolumbo seamount (Aegean Sea) in Greece (Ulvrová et al., 2016). The above examples show that the study of the instability of volcanic seamounts and potential tsunami generation is of primary importance to evaluate (a) the exposition of coastal areas to this type of hazard and (b) the impact on the population and infrastructures. Therefore, an analysis of stability is required as a first step approach to verify the present-day potential destabilization of the flanks of submarine volca-noes and the ability of the consequent sliding to generate tsunamis.

The southern Tyrrhenian Sea is a 2 Ma old back-arc basin associated with the northwestward subduction of the Ionian Sea below the Cala-brian Arc (Malinverno and Ryan, 1986; Faccenna et al., 2007). The Tyrrhenian back-arc includes 33 censored volcanic seamounts (Pensa et al., 2019) mostly located north of Sicily and west of Calabria. Sea-mounts concentrate in the submerged portion of the Aeolian volcanic Arc (Fig. 1). The northern termination of the Ionian slab consists of an E-W strike-slip fault system separating the continental crust from the oceanic crust of the back-arc basin. The about 70 km long Palinuro vol-canic chain (PVC) emplaces along with this fault system and consists of 15 E-W aligned volcanoes with height up to 3200 m from the seafloor (Cocchi et al., 2017) (Figs. 1 and 2). The occurrence of calderas (to the west), slide scars, and incised canyons provide evidence of instability phenomena (Passaro et al., 2010). Also, PVC is affected by hydrothermal activity that can weaken the volcanic rocks (e.g. Caratori Tontini et al., 2010, 2014; Szitkar et al., 2015) and by crustal and deeper earthquakes with magnitude up to 5 (Rovida et al., 2019). Shallower seismicity possibly related to hydrothermal activity has been also detected (Soloviev et al., 1990).

Based on these data and depending on the characteristics of col-lapses, the PVC poses a potential tsunami hazard problem also consider-ing the proximity of the coast of Italy mainland and the Aeolian Islands, which are in a radius of less than 100 km from the Palinuro volcanoes. Here, we provide a stability analysis of the PVC related to earthquake oc-currence and tsunami simulations by selecting different unstable flanks of the volcano. Our approach consists in (a) identifying zones of PVC with morphological or geophysical evidence of past seafloor mass movements or potential weakness zones as the morphological wedges, (b) performing a stability analysis from distant tectonic earthquakes and proximal volcanic earthquakes based on PGA values, and (c) simulating the potential tsunami triggered by mass movements. Therefore, our study does not focus on the simulation of well-established past mass movements, but it analyzes the present-day instability of PVC and the potential effects of tsunami associated with seafloor sliding activated by seismic shaking. Our results have im-plications for the evaluation of tsunami hazard in the southern Tyrrhenian Sea.

2. Geological setting

PVC is a large, E-W striking volcanic ridge located in the SE Tyrrhenian Sea. The volcanic chain lies at the northern boundary of the Marsili extensional back-arc basin, emplaced by the Ionian litho-sphere subduction below the Calabrian Arc in the context of the Africa–Eurasia convergence (Malinverno and Ryan, 1986). Petrological
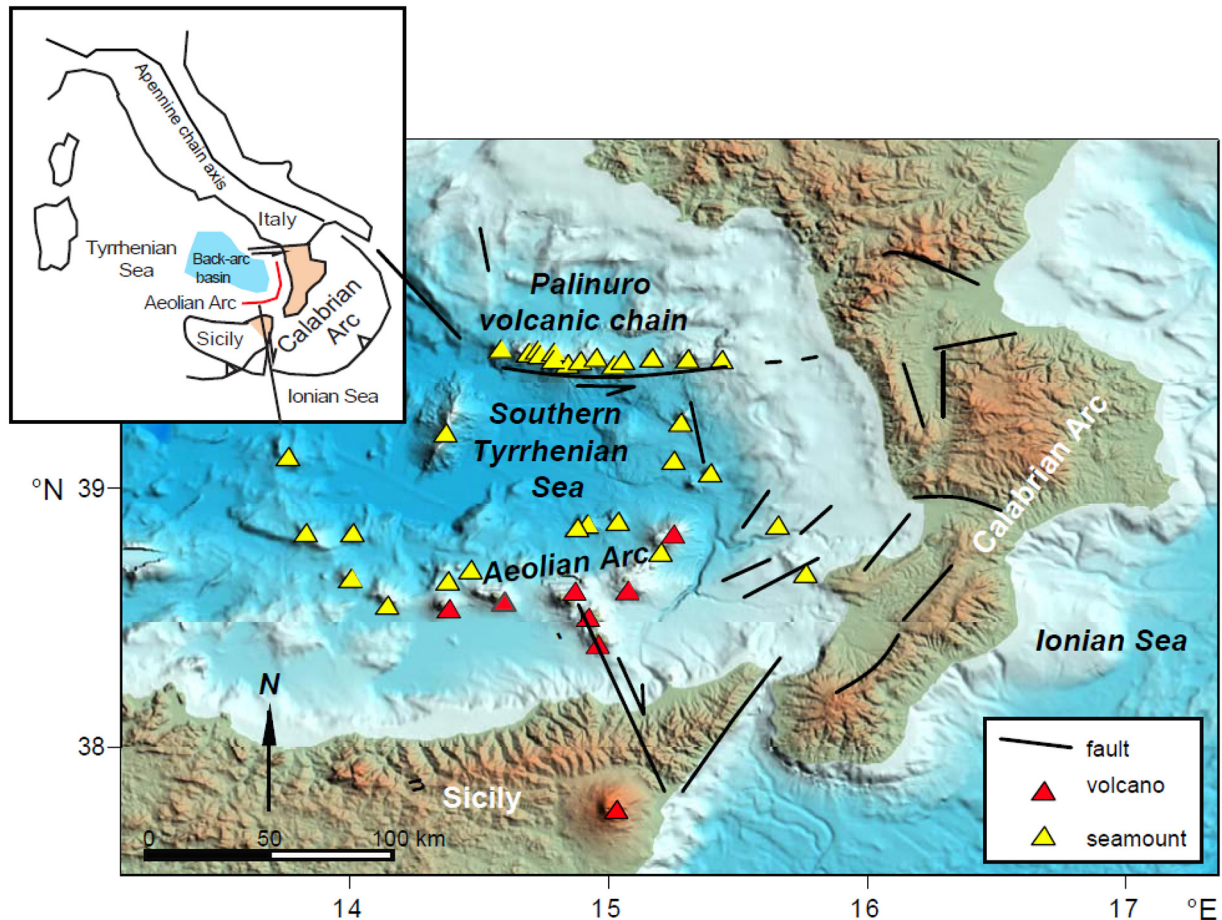

Fig. 1. Geodynamic setting of the Calabrian Arc – Ionian Sea subduction (inset), and distribution of faults, subaerial and submarine volcanoes in the southern Tyrrhenian Sea (data from Malinverno and Ryan (1986), Faccenna et al. (2007), and Cocchi et al. (2017)).
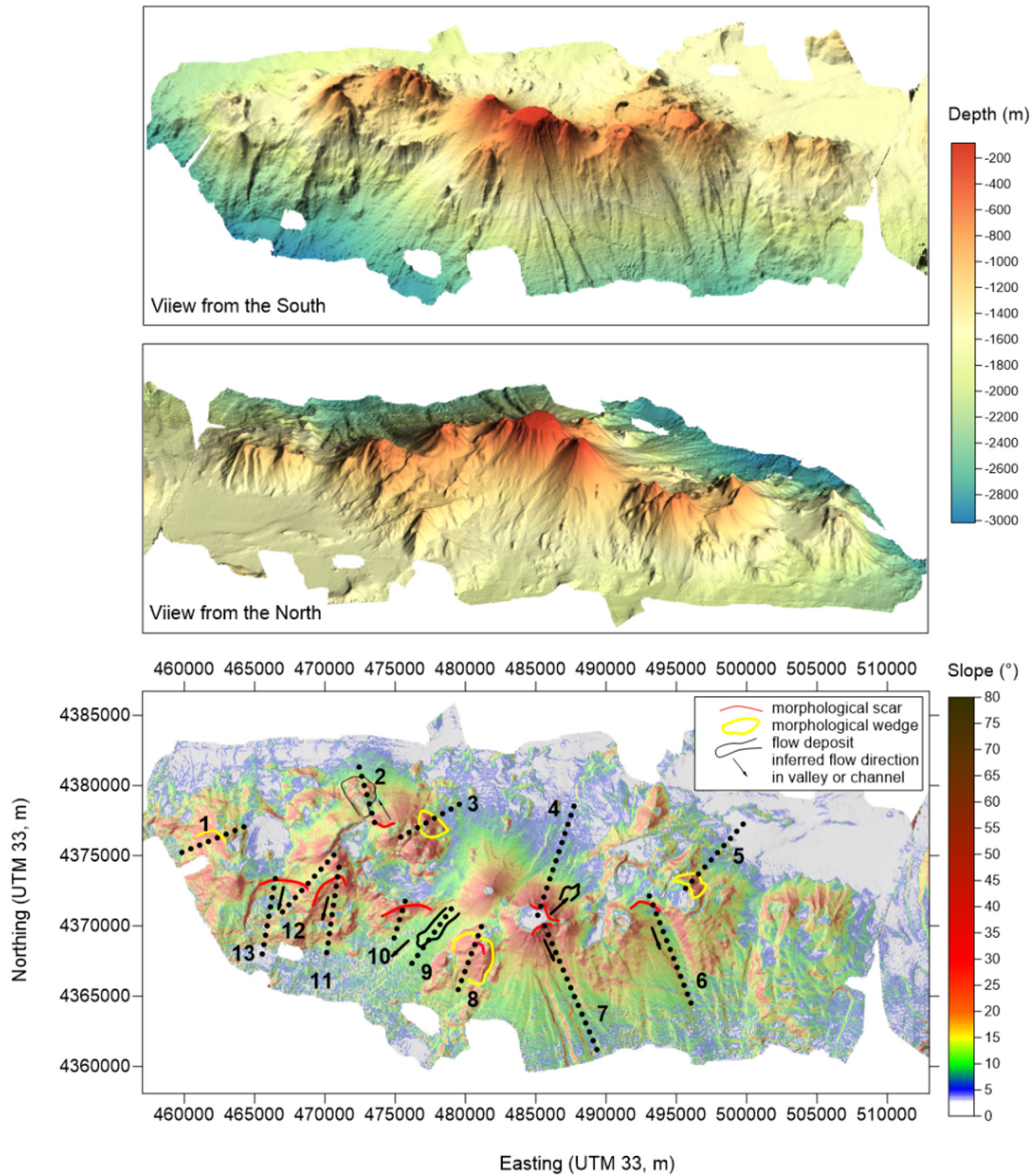
Fig. 2. View from the north and south of the Palinuro volcanic chain (top) and slope map superimposed to a shaded-relief DTM (bottom). The main morphological evidence of past landslides (scars, accumulated flow deposits) and potentially unstable structures (morphological wedges) are also reported along with the profiles selected for the stability analysis. Datum is WGS84 UTM 33.

studies based on bottom sampling demonstrated that the PVC was emplaced over a relatively long time interval (not less than 0.5 Ma; Colantoni et al., 1981; Beccaluva et al., 1985), and revealed the presence of lavas and sediments associated with hydrothermal vents (i.e. crusts and iron- and manganese-bearing nodules; Dekov and Savelli, 2004 and references therein).

The overall PVC alignment has been interpreted as the morpho-structural consequence of an E-W striking strike-slip fault system (e.g., Colantoni et al., 1981; Guarnieri, 2006; Del Ben et al., 2008; Milano et al., 2012). According to Guarnieri (2006) and Cocchi et al. (2017), the PVC emplaces over a lithospheric fault linked to the

northward tear fault of the Calabrian-Arc subduction (i.e., the Subduction Transform Edge Propagator, or STEP). Cocchi et al. (2017) demonstrated that the STEP fault-related magmatic activity at the PVC ridge is larger than that observed in the back-arc and Aeolian Arc. Active seismicity and hydrothermal vents characterize the PVC ridge (Soloviev et al., 1990; Lupton et al., 2011). In recent times, several studies pointed out the presence of potential mining resources linked to hydrothermal vents on the PVC chain (Lupton et al., 2011; Ligi et al., 2014; Safipour et al., 2017). Hydrothermally altered rocks, lateral and vertical compositional inhomogeneity of the edifices, that are typical of volcano buildings (e.g. Thouret, 1999), and rapid slope changes due to marine

abrasions (Passaro et al., 2011a) are all potential triggering factors of large flank instabilities.

The PVC is made up by the coalescence of several volcanic edifices joined in an up to 3200 m high elongated morphological ridge. Geophysical (Caratori Tontini et al., 2009) and geomorphologic studies (Passaro et al., 2010) demonstrated that the PVC volcanic features are organized in clusters grouped by a similar volcanic evolution history, probably related to previous or subsequent stage of emergence or to large differences in crustal thicknesses (McPhie, 1995). Caldera morphologies characterize the westernmost PVC sector, flat-top cones are present in the central sector, and fracture-controlled edifices are located in its easternmost area (Passaro et al., 2010, 2011b). The northern and southern flanks of the PVC ridge have asymmetric slopes, both characterized by canyons and slide scars that drive sediment movements. The PVC northern flank has an average slope of 18° and the base level is located at 1600 m below sea level (Palinuro Basin), while the southern flank shows 20 ° — 30°slope values and reaches a depth of ~3200 m. At this depth, the slope changes drastically to 2°, that is the average value of the northern sector of the Marsili Basin abyssal plane. Backscatter images of the PVC apical sector show several changes in sediment coverage with local exposure of volcanic rocks (Innangi et al., 2016).

3. Data and methods

3.1. Geophysical data

Multibeam data acquisition was carried out in the frame of the "Aeolian_2007" oceanographic cruise onboard the Urania oceanographic vessel operated by the National Research Council (CNR) of Italy. Data were collected by a Reason Seabat 8160 multibeam sonar system, suitable for acquisition of bathymetry in a depth range of 50 – 3500 m. The multibeam system, interfaced with a Differential Global Positioning System, operates at 50 kHz with 126 receiver beams and an aperture of 150°. Sound velocity profiles were acquired every 6–8 h during the survey and were supplied to the system for the beam forming. A final Digital Terrain Model (DTM) was obtained after tidal correction and de-spiking using the PDS2000 grid tools and covering ~1000 km^2 of the seafloor morphologies (min/max depths are −84 m/−1200 m) (Fig. 3). Further details are reported in Passaro et al. (2010). Multichannel reflection seismic lines were acquired during the 2010 TIR10 cruise (Doglioni et al., 2012). The seismic source used was a tuned array of three SERCEL GI-GUN (2 × 45/45, 75/75 in^3), towed at a depth of 5 m and operating at a pressure of 140 bar. The seismic receiver was a 1200 m-long 96-channels SERCEL digital streamer with a group interval of 12.5 m and towed at a depth ranging 4 to 7 m. The shot interval was set at 37.5 m distance travelled allowing a fold of 1600%, while the sampling rate was 0.5 ms with a record length of 12 s. Seismic data were processed for the purpose of our work using an industrial package (Disco/Focus) by Paradigm Geophysical, following a non-standard sequence, with the aim of obtaining depth-migrated sections. Processing includes: swell noise removal; setting of acquisition geometry; interactive noisy trace editing; spherical divergence correction; predictive deconvolution; time variant band-pass filtering; CMP sorting and velocity analysis; random and coherent noise reduction by f-k and tau-p velocity filtering in the shot, receiver and common midpoint domains; bottom surface multiple removal using 2D surface related multiple suppression (SRME) technique and adaptive filters; normal move out (NMO) and dip move out (DMO) corrections; NMO removal and velocity analysis; NMO and stacking; and finite difference depth migration after iteratively smoothing and refining the velocity model (Fig. 3; for further details, see also Ligi et al., 2014).

3.2. Numerical modelling

This study includes analyses and simulations from numerical models that have been widely applied for the reconstruction of landslide or
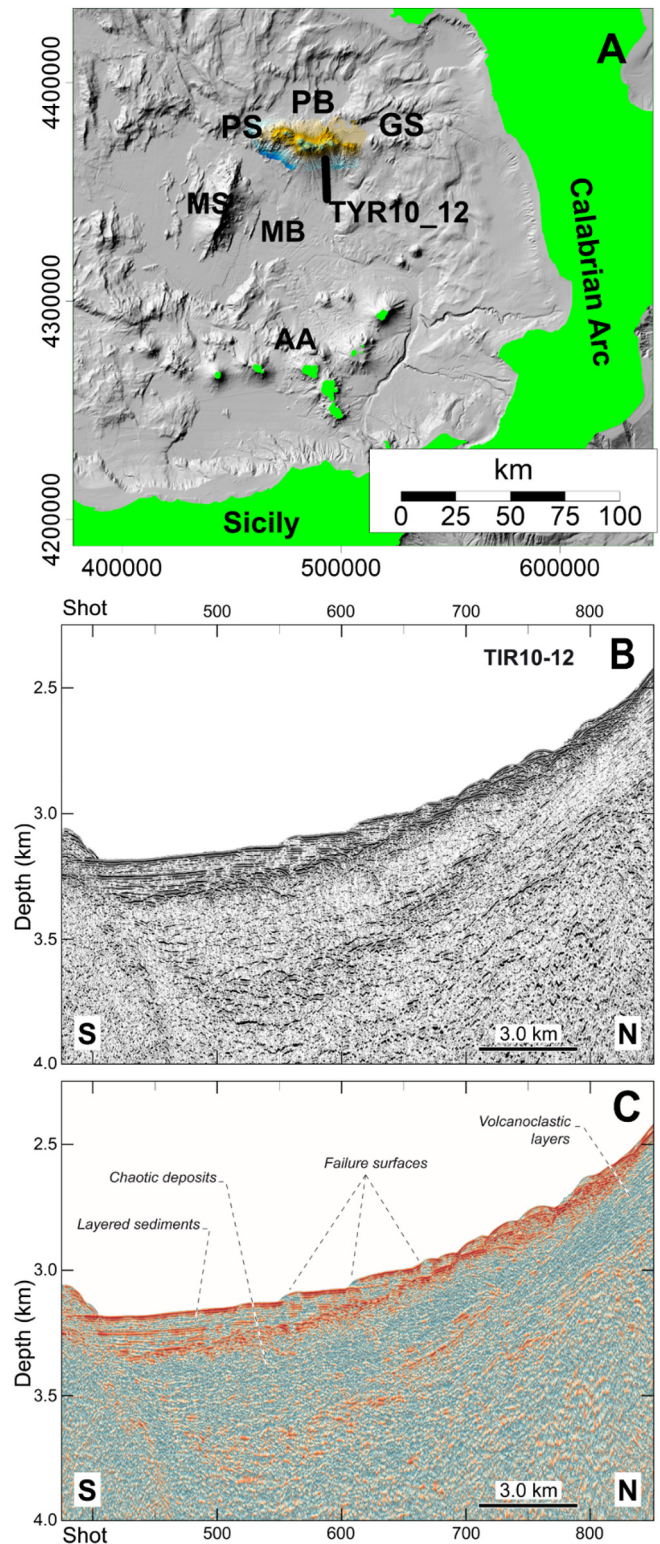

Fig. 3. A) Location map of the PVC and TYR10_12 multi-channel seismic profile. GS = Glabro Seamount, PB = Palinuro Basin, MB = Marsili Basin, MS = Marsili Seamount, AA = Aeolian Arc. B) Uninterpreted portion of depth migrated seismic line TIR10–12 showing details of sedimentary deposits at the base of the PVC. C) Instantaneous amplitude (envelope) providing information on reflection strength and lateral continuity of seismic reflectors.

landslide-tsunami events (Tinti et al., 2011; Zaniboni et al., 2013; Zaniboni et al., 2014; Zaniboni and Tinti, 2019). The stability analysis on PVC has been carried out to determine the sectors associated to potential mass movements by employing the minimum lithostatic

deviation (MLD) method. This 2D revised technique (Tinti and Manucci, 2006, 2008) of the classic limit-equilibrium method (LEM) was applied to determine the stability of a sector of Mt. Nuovo (Ischia Island) under the effect of seismic loading (Paparo and Tinti, 2017). The analysis can be performed on single or multiple cross-sections of a landslide body. For this purpose, the 3D body can be divided in a specific number of sections where the limit equilibrium conditions are imposed considering the main forces acting on the system. These are the vertical and horizontal components of the inter-slice forces, the normal and shear stresses acting on the bottom of the section, the weight, and the external load. This latter can be considered in terms of the water pressure (for submerged slopes) and/or the seismic load induced by an earthquake (considered in terms of Peak Ground Acceleration). Here, we assume that typical seismic loads induced by volcanic earthquakes affect the weakest sectors of PVC. In the model approach, the material forming the slope is assumed to obey the Mohr-Coulomb failure criterion, reckoning the maximum shear strength that the slope can withstand to remain stable. When this value is exceeded, the landslide base becomes unstable inducing the slope failure. Commonly, this condition is reached when the so-called factor of safety F has values lower than 1. F is defined as the ratio between the limit shear strength and the shear stress at the base of the selected landslide section. The conventional LEM formulation leads to a set of differential equations that cannot be uniquely solved, but several techniques allow its solution in 2D (e.g. Janbu, 1973; Sarma, 1979) or 3D configurations (see Kalatehjari and Ali, 2013 for a review). Here, the MLD method ensures a unique solution for the set of equations by imposing a principle of minimization. Several values of the F factor are tested until the minimum value of the lithostatic deviation is reached. This latter is given by the ratio between the average value of the inter-slice forces and the total load exerted by the landslide body. A set of technical parameters defining the soil characteristics is required to evaluate the F factor, namely the slope friction angle, the average soil cohesion, and the landslide body specific weight. The choice of the profile shape and depth can be reconstructed from seismic profiles (where available) or hypothesized following geological considerations.

The initial sliding areas are located following the results of the stability analysis, implying local geomorphological considerations (see Section 4.1 and Fig. 2). The motion of the slide is then computed by utilizing two distinct numerical models. In this work, the landslides simulations have been considered related to the potential tsunami generation. Thus, no attention has been given to the final deposits since they are irrelevant in the tsunami triggering process, which is restricted to the accelerating phase of the motion (Enet and Grilli, 2007; Løvholt et al., 2015). Then, the sliding process is reproduced through a block-based model (UBO-BLOCK2) and a Depth-Averaged Flow (UBO-DAF) model. The former, adopting a Lagrangian approach, divides the sliding body in a set of interacting blocks that can change shape during the motion but preserve their volume. The UBO-BLOCK2 tool has been specifically designed to describe the input that the slide gives to the water as it moves downslope. Further details regarding the equations of motion and the set of parameters required by the model can be found in Tinti et al. (1997). The other depth-averaged model adopted to provide reference results of the landslide dynamics is derived from the Navier-Stokes equations using the shallow-water approximation. It incorporates the rheology of a Mohr-Coulomb model (Savage and Hutter, 1989) and the modification from topography effects for a global Cartesian coordinate system (Xia and Liang, 2018). Buoyancy and drag forces are included in the model to account for the effects of water on the submarine landslides. The UBO-DAF model, accounting for mixture debris flow, was previously applied for the reconstruction of the 1783 Scilla landslide, Italy (Wang et al., 2019), in which the landslide deposits well fit the observations.

The tsunami generation is evaluated from the block-based model results. As a matter of fact, for 2D slides, more complex and realistic events can be related to a simplified rigid-body motion (Enet and Grilli, 2007).

The UBO-BLOCK2 output can be adopted to estimate the energy given to the column of water by employing the UBO-TSUIMP code. This latter accounts for the upward shift of the water mass due to the landslide. A filtering technique is applied to attenuate wavelengths smaller than the local sea depth. The output of this procedure is a time-dependent tsunami impulse suitable for waves generated by landslides. Hence, the tsunami propagation is computed through the UBO-TSUFD model, which solves the Navier-Stokes equation by finite differences in the shallow water approximation. The code can handle systems of nested grids at a specific level of nesting and accounts for the linear and non-linear terms. Pure transparency conditions are applied to the open external boundaries while different conditions can be selected along the coastlines: (a) a moving boundary technique is adopted when considering tsunami inundation or (b) a rigid vertical wall is assumed when pure wave reflection has to be considered. A detailed description of the numerical code can be found in Tinti and Tonini (2013).

The adopted regular computational grids for both the landslide models are 50 m spaced and are obtained from the EMODnet database (https://www.emodnet-bathymetry.eu/, EMODnet Bathymetry Consortium, 2018). A finer grid (25 m spaced) provided by Passaro et al. (2010) embraces the upper sections of the seamounts (see Fig. 2) and has been used for the stability analysis. The UBO-TSUIMP model runs on a 250 m regularly spaced domain obtained by interpolation of the above mentioned EMODnet dataset. The tsunami propagation is computed over a 750 m spaced grid, covering the entire Tyrrhenian Basin (591×432 km^2) with 450,000 nodes.

4. Results

4.1. Geomorphological and geophysical evidences of gravity instability

The morphological analysis of the DTM reported in Fig. 2 shows that PVC is characterized by some slide scars concentrated on the flat top of the Palinuro seamount and the flanks of the edifices localized in its western sector. The scars affecting the top of the Palinuro Seamounts cut the marine terrace flat landform probably formed during the Last Glacial Maximum (Passaro et al., 2010, 2011a, 2011b). Therefore, the age of these scars is younger than about 18–20 ka. Geochronological constraints are lacking for the other recognized scars. Evidences of mass movements are given by well-defined mass flow accumulation features (Fig. 2), whose volumes range between 0.7 and 0.2 km^3. However, the age of such mass depositions is unknown and, in addition, there are no data to discriminate the emplacement mechanism, i.e. single vs. polyphase emplacement. Wedge-like morphological structures have been also recognized (Fig. 2). Although such structures do not reflect instability processes, however, by analogy with continental volcanoes, they may be affected by future sliding due to seismic shaking (Bisson et al., 2018). The maximum volume of such wedge-like morphologies is 0.80 km^3. The seismic image of Fig. 3 shows clear evidence of failure surfaces and associated gravity sliding deposits and highlights chaotic material beneath well stratified sediment layers, suggesting large mass wasting from the flanks of the PVC in the past.

4.2. Stability analysis

Morphologic inspection of the PVC bathymetry suggests 13 profiles (Fig. 2) as possible loci of mass movements on its flanks. The seismic profile in Fig. 3 shows a ~150 m-thick sedimentary cover on its apical sector. This profile is located in one of the valleys/gorges surrounding the complex, where ejected materials were naturally accumulated during past eruptions. Consequently, we have focused the attention on these zones excluding ridges and dikes. The stability profiles are centered in the valley innermost sections since the destabilization of such areas could eventually lead to mass failures. The maximum depth of the corresponding cross-sections is in the order of $100 - 150$ m, following the shape of the only available seismic profile. Hence, it is assumed

that loose materials cover analogous zones of the seamount in a similar way. This approach seems reasonable because of the numerous, partly juxtaposed PVC edifices. Indeed, small perturbations around this thickness' values would not influence considerably the analysis here performed.

Stability analysis is carried out including the effects of internal seismic loading and the external water load. Since no seismogenic tectonic structures are known in the PVC area, one should consider the ground motion variations induced by earthquakes occurring on the well-known active faults of the Apennines chain in the Italy mainland. By adopting characterizations of expected PGA for such typical seismic sequences (e.g. Malagnini et al., 2008), negligible PGA values are found in the PVC area. Due to the considerable distance from the chain (>200 km), even the strongest historical earthquakes in the surrounding regions are not able to produce evident effects.

On the contrary, shallow volcanic earthquakes are rather common on volcanoes, and they could be more relevant for the PVC case-study (see McNutt and Roman, 2015 for a review). Shallow seismic waves dissipate faster with respect to the deeper ones but induce higher PGA values in the epicentral area (Lanzano and Luzi, 2020). Although shallow seismicity is present on the PVC, earthquakes from this area are scarcely observed from the Italian network of seismic monitoring due to the rapid waves amplitude attenuation of these shallow events. This aspect could explain the absence of recorded events on the PVC in the seismic databases, given that no seismic stations are located on the seamounts. However, the occurrence of shallow seismicity on the Tyrrhenian seamounts has been widely observed in oceanographic missions (D'Alessandro et al., 2009). Ocean-bottom seismometers placed on the easternmost sector of the PVC in 1987 recorded tens of shallow volcano-type microearthquakes (M < 3) in less than two weeks (Soloviev et al., 1990).

The estimation of the PGA at a given distance r from the epicenter depends on the nature of the earthquake and on the soil characteristics. For shallow (<5 km), low-frequency events, the logarithmic relationships are estimated as follows (Sabetta and Pugliese, 1987; Ambraseys et al., 1996; Tusa and Langer, 2016):

$$\log(PGA) = a + bM + c\,Log\left(\sqrt{r^2 + h^2}\right) + e_i S_i \qquad (1)$$

where a, b, c, h are site related coefficients and generally match the observations, e_i depends on the soil type, S_i represents the soil conditions (0 wet, 1 dry), and r is the epicenter distance. According to the Eurocode classification (CEN, European Standardization Committee, 2003), only two of the eight classes provided are typical of volcanic sites: a) hard rocks, such as volcanic (lavas) and plutonic rocks and/or lithified marine deposits; and b) metamorphic rocks and sediments. Herein, the PGAs are considered for a typical range (Tusa and Langer, 2016; Lanzano and Luzi, 2020) of volcanic earthquakes ($3.6 < M < 4.8$) and for two reference epicentral distances $r_1 = 1$ km, $r_2 = 5$ km. The values of the coefficients are chosen following Tusa and Langer (2016):

a = −1.183 b = 0.724 c = −1.716 h = 1.541 e_A = 0 e_B = 0.359

These values are calculated based on a database that virtually matches the classes of earthquakes expected on the PVC. The results are shown in Table 1.

To assess a realistic stability analysis, specific technical parameters should be determined for each profile. Given the lack of detailed information about the loose materials covering the PVC flanks, the relevant mechanical and geotechnical parameters have been selected referring to similar structures, though they are known to cover a broad range in submarine sand/or volcanic areas (see Seisdedos et al., 2012; Schaefer et al., 2015, and references therein). Based on the specific environment, the evidence of loose material from the seismic profile (Fig. 3), and results from previous studies (del Potro and Hürlimann, 2008; Apuani

Table 1
PGA values (in percentage of the gravity acceleration g) at $r_1 = 1$ km and $r_2 = 5$ km distances, computed through Eq. 1 for Eurocode 8 soil classes A and B.

M	PGA (e_A) r_1	PGA (e_B) r_1	PGA (e_A) r_2	PGA (e_B) r_2
3.6	0.009	0.022	0.001	0.004
3.8	0.013	0.030	0.002	0.005
4.0	0.018	0.042	0.003	0.007
4.2	0.025	0.059	0.004	0.010
4.4	0.036	0.082	0.006	0.014
4.6	0.050	0.115	0.008	0.019
4.8	0.070	0.160	0.011	0.027

and Corazzato, 2010; Schaefer et al., 2013; Schiffman et al., 2006; Harnett et al., 2019), a set of values have been selected (Table 2).

The stability analysis has been performed for the range of parameters shown in Table 1. For the sake of simplicity, only PGA values equal to $0 − 0.05 − 0.10 − 0.15$ have been evaluated, bearing in mind that these values can only be reached just in the vicinity (1 km) of a seismic event. Lower values are insufficient to destabilize the slopes. It is also assumed that the entire profile is subject to the same load. The analysis reveals four profiles (1, 7, 11, and 12) with values of F lower than 1 in some configurations. Fig. 4 shows plots of PGA vs. F for the profiles 1, 7, and 11. These have been selected as the initial sliding areas for the mass failures scenarios. Due to the proximity of profiles 11 and 12, only one scenario has been reconstructed in this sector. Results from the complete analysis are shown in Table A1 in Appendix A.

4.3. Mass failures

The potentially unstable profiles highlighted by the stability analysis are located in 3 distinct sectors of the PVC. The reconstruction of the sliding volumes follows the local geomorphological features and the information from the seismic profile. In particular, the hypothesized sliding volumes vary on different orders of magnitude to analyze the related scale of the triggered tsunami. The sources of mass failures (P1, P2, and P3 in Fig. 5) cover areas of 7 km², 14 km², and 25 km², respectively. They are bounded by the natural edges of the specific valley and have elongated shapes. The average thickness is 40 m in the P1 case, and 100 m for P2 and P3 with corresponding slide volumes of 0.7 km³, 1.5 km³, 2.4 km³, respectively. A basal friction coefficient $\mu = 0.05$ is assumed, based on a set of landslide parameters adopted by Kelfoun et al. (2010) in a similar environment. As outlined in the previous section, the landslide evolution has been computed by two numerical codes (UBO-BLOCK2 and the UBO-DAF model). Here, we show the dynamics computed by the two models in terms of the velocities of the slide Center of Mass (CoM). We focus on the initial part of the motion, which is the most relevant for tsunami generation. Fig. 6 shows the CoM velocity curves for the three simulated slides. Velocity peaks are in the order of 60 m/s for all the UBO-BLOCK2 simulations. The UBO-DAF model results show slightly lower maxima and a similar path in the accelerating phase of the motion. We observe that the slides decelerate at longer times when bodies move slowly in deep water. However, this is irrelevant for the tsunami generation. In all the simulations, the slides reach their maximum speed in the first two minutes.

Table 2
Sets of values adopted for the stability analysis (ϕ is the friction angle, c the cohesion and γ the rock unit weight).

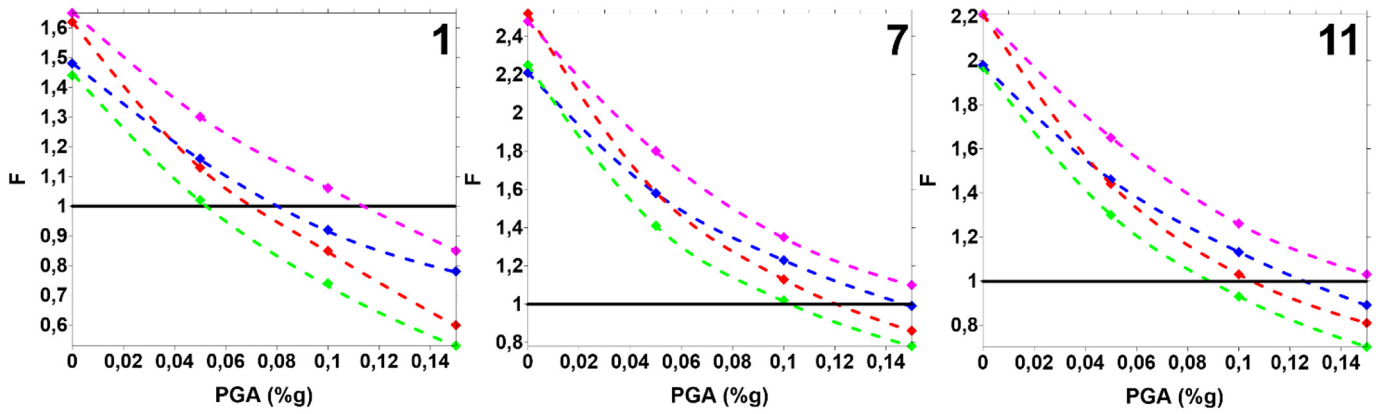| Set	ϕ (°)	c (kPa)	γ (kN/m³)
s_1	30	5	20
s_2	30	5	15
s_3	33	5	20
s_4	33	5	15

Fig. 4. Stability curves for profiles 1, 7, and 11 (see Fig. 2). Blue, green, magenta, and red dashed lines denote results for the s_1, s_2, s_3, and s_4 sets of parameters, as listed in Table 2. The black line marks the stability-instability transition ($F = 1$). (For interpretation of the references to color in this figure legend, the reader is referred to the web version of this article.)

4.4. Tsunami generation and propagation

The tsunami forcing term due to the motion of the submarine landslides is computed by the code UBO-TSUIMP and forms the input, variable in space and time, for the tsunami propagation code UBO-TSUFD. In each node of the tsunami computation grid involved by the landslide motion, the code UBO-TSUIMP provides the induced change of the sea surface level.

Tsunamis with different magnitudes are generated by the three hypothesized scenarios and propagate across the Tyrrhenian Sea. We have studied their radiation in the central and southern part of the basin where their waves are larger and show the simulation results through a series of plots. Sea surface maxima computed for the first 2-hour propagation time are depicted in the panels of Fig. 7, which covers the SE Tyrrhenian Sea. The upper panels refer to the smallest landslide volume (case P1, volume 0.7 km^3) and show extreme values within 20 cm revealing that such PVC sources are able to produce minor tsunamis. Conversely, the P2 and P3 scenarios show extreme values in the order of 1 m and 5 m, respectively. These scenarios are worthy of consideration as regards hazard and risk analyses. Maxima are not symmetrically distributed around zero. Close to the source, troughs' magnitudes prevail on the crests. At larger distances, differences tend to reduce.
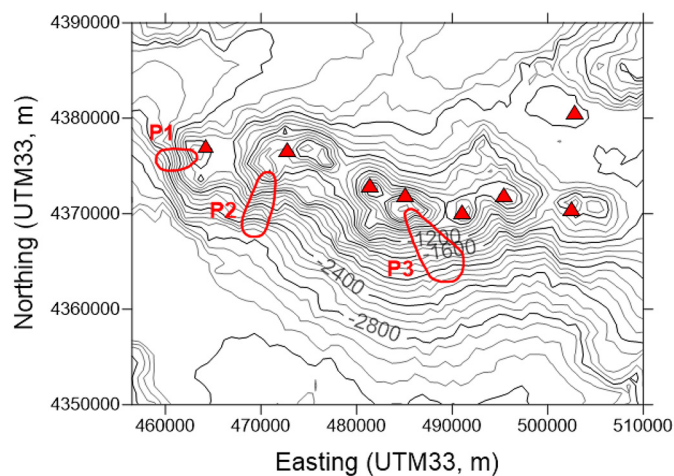
Interestingly, the tsunami propagation pattern is far from being isotropic. Instead, it is characterized by a strong concentration of tsunami energy along some preferential directions. This depends on the tsunami sources, but also on the bathymetry that influences the phase velocity of the waves. When a front incurs in linear high-slopes submarine structures like ridges or seamounts, then the refraction induces wave focusing with the consequent formation of high-amplitude beams that can persist for long distances and up to the coast. This effect was documented for the 2004 Sumatra megatsunami propagation across the global world ocean (see Titov et al., 2005; Kowalik et al., 2007; Rabinovich et al., 2017). In the case of the PVC tsunami scenarios, i) the Marsili seamount, ii) the E-W trending lineament including PVC, the Glabro seamount and the offshore-protruding margin in front of Cetraro Marina (northern Calabria), as well as iii) the structural high in the northern sector, are responsible for the three main beams running southward (or southwestward), eastward and northward from the source region, respectively. It is worth noting the effect of the Marsili seamount (Fig. 1) on the three tsunamis. In all cases, the steep slopes of the Marsili edifice create a well-delineated beam but, depending on
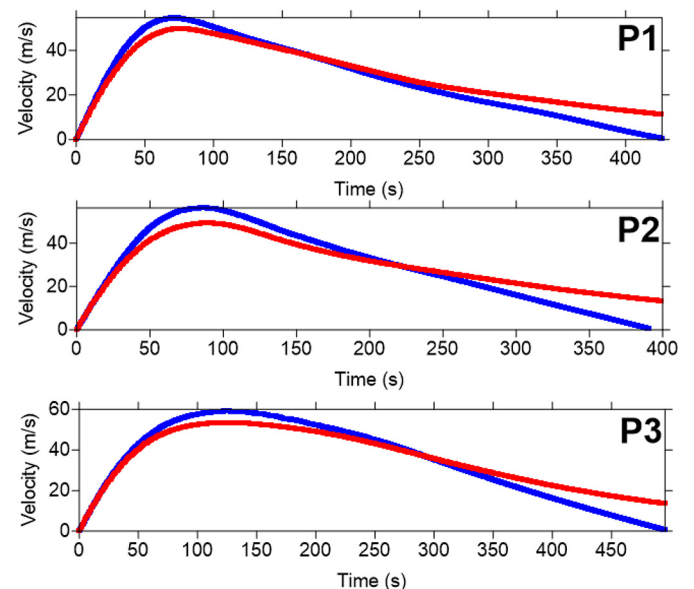

Fig. 5. Initial sliding areas are delimited by red lines for the three simulations (P1, P2, and P3). These areas have been selected following the stability analysis carried out over the profiles in Fig. 4. Red triangles mark the summit of volcanic edifices. (For interpretation of the references to color in this figure legend, the reader is referred to the web version of this article.)

Fig. 6. CoM velocity time histories from UBO-BLOCK2 (blue lines) and UBO-DAF (red lines) models. Notice that the acceleration phases are similar. Relevant discrepancies are only in the final part of the motion. (For interpretation of the references to color in this figure legend, the reader is referred to the web version of this article.)
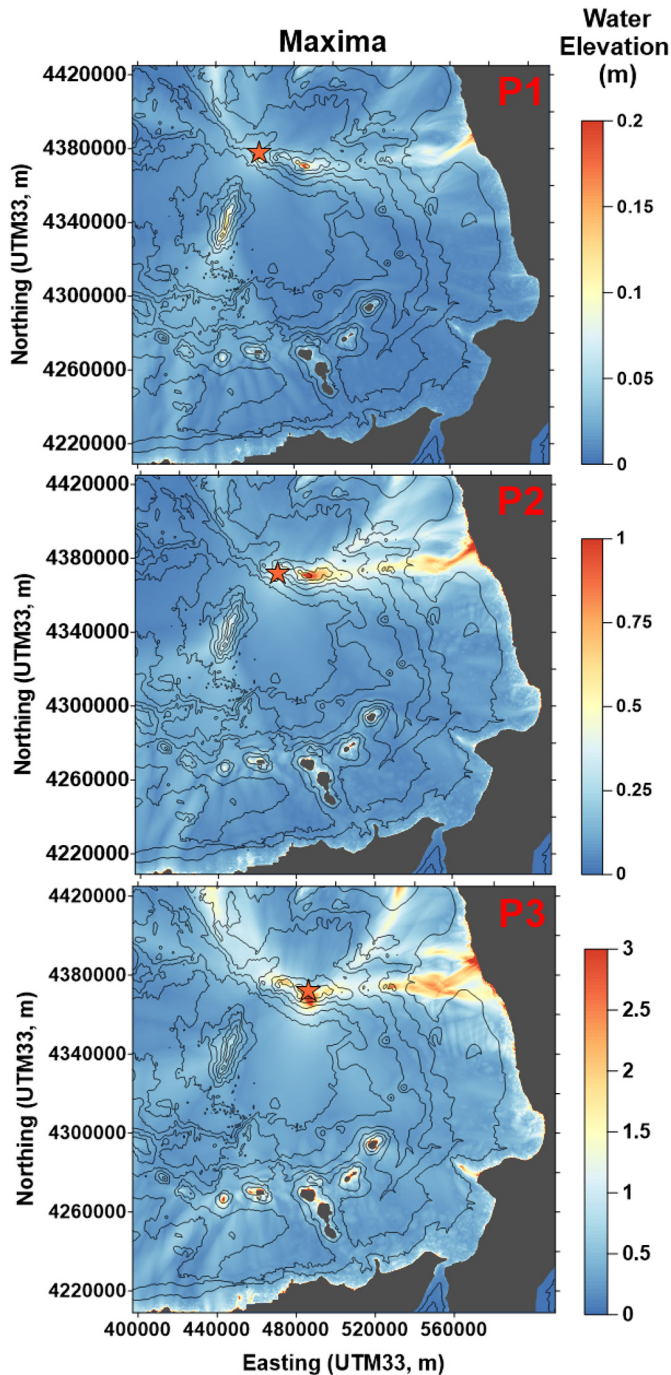
Fig. 7. Maximum water elevations in the P1, P2, and P3 scenarios over the south-eastern sector of the Tyrrhenian Sea. The orange stars denote the initial sliding areas. Note that the palette saturates at different values in the three cases.

compared to tsunamigenic faults that may extend for hundreds of km. Further, we note that the tsunami advances with a positive leading front along the direction of the landslide motion, and with a negative one in the opposite direction. More specifically, if we restrict to the case P3 (lower panels of Fig. 7) for illustrative purposes, we notice that, at the beginning, the main positive front moves towards SE coherently with the movement of the landslide (see Fig. 5), while the main negative front moves NW-ward. This feature can be considered the signature of the source. At later times, the bathymetric configuration of the basin may prevail as a conditioning factor. A further consideration is that the snapshot sequence confirms the refractive bending of the fronts induced by the above-mentioned bathymetric highs. As for the tsunami lead time, we see that the waves reach the coasts extending from southern Campania to northern Sicily in about 15–20 min, with first arrivals in southern Campania.

The tsunami elevations along the coast are displayed in Figs. 9 and 10. They are computed offshore, along the 10 m depth isoline, and, considering the space resolution adopted in the simulations, they provide a reliable low-resolution picture of the tsunami behavior in the coastal regions. Local flooding analysis and detailed run-up heights evaluation require much finer space grids with a consequent huge increase in computer resources. This development is left for future investigations. The tsunami-related heights of the sea-surface affecting the eastern coast of the basin (from Campania to Calabria) are generally of ~0.5 m, ~0.4 m along the southern coast (Sicily) and ~0.2 m along the western coast (Sardinia) (Fig. 9). Similarly to the distribution of the wave amplitudes, the height peak around 1.5 m in northern Calabria corresponds to the E-W beam aligned with the PVC (see upper panels of Fig. 7). Similar reasoning can be made for the coastal sea-surface elevations of the P3 case depicted in Fig. 10, taking into account, however, that the tsunami amplitudes are much higher. Sea-surface elevations are ~2 − 2.5 m on the eastern coast, ~2 m on Sicily and ~0.4 − 0.6 m on Sardinia. The peak in correspondence of the coast of the eastward-moving beam is as high as 6 m. In addition, two more peaks are worth of notice: one of ~4 m at Vaticano Cape (southern Calabria) and the other with an elevation of ~3 m at Mondello Cape, to the west of Palermo town, Sicily. These peaks are due to the local effect of near-coast wave-focusing induced by the two promontories.

5. Discussion

Our results evidence that the PVC could be potentially affected by sliding phenomena related to shallow, low magnitude volcanic earthquakes. Such sliding movements are able to trigger tsunamis whose effects on the coast of the Campania, Calabria, and Sicily regions may be relevant. Our assumptions about the sliding volumes are related to the thickness of loose material revealed by the seismic profile in Fig. 3, which is close to the location of Profile 7 (simulation P3). The slide dynamics is computed by employing two distinct numerical models and by adopting a strategy that provided satisfying results (Kirby et al., 2016). The models provide consistent results in terms of velocity time histories (Fig. 6). This is an interesting result in the framework of landslide-generated tsunamis because the advantages and limitations of the two approaches are still debated (Løvholt et al., 2015; Yavari-Ramshe and Ataie-Ashtiani, 2016). However, the obtained results are different in the decelerating phase of the motion. This is mainly due to the way the models adopt in computing the drag forces exerted by the water. Nevertheless, this aspect was not subjected to further investigation since a detailed description of the slide trajectory and deposits is not the object of this study. The lack of detailed information about the PVC does not allow us to perform specific sensitivity analysis on the basic parameters the numerical model requires. This is particularly true for the landslide simulations. As known, landslides induce alterations in the water level. The amount and extent of such alterations reflect differences in the sliding volume. At the PVC, the P1 scenario produces the lowest effects on the water basin and large waves are

the relative position with respect to the source, the beam orientation changes and rotates from SSW (for P1) to SW (for P3). Worth of mention is also the effect of the arc of the Aeolian islands on the tsunamis. Waves are diffracted around the islands which, being of volcanic origin, have the shape of elongated cones. Altogether, the Aeolian Islands form a semi-permeable barrier crossable by the tsunami, although with great loss of energy.

The evolution of the wave fronts is shown only for the most relevant tsunamis (cases P2 and P3) in Fig. 8 through field snapshots taken at six instants from 1 to 30 min. Propagation patterns are similar and characterized by an initial radial spreading; this feature is typical of landslide-tsunamis, i.e., tsunamis generated by limited-extent sources as
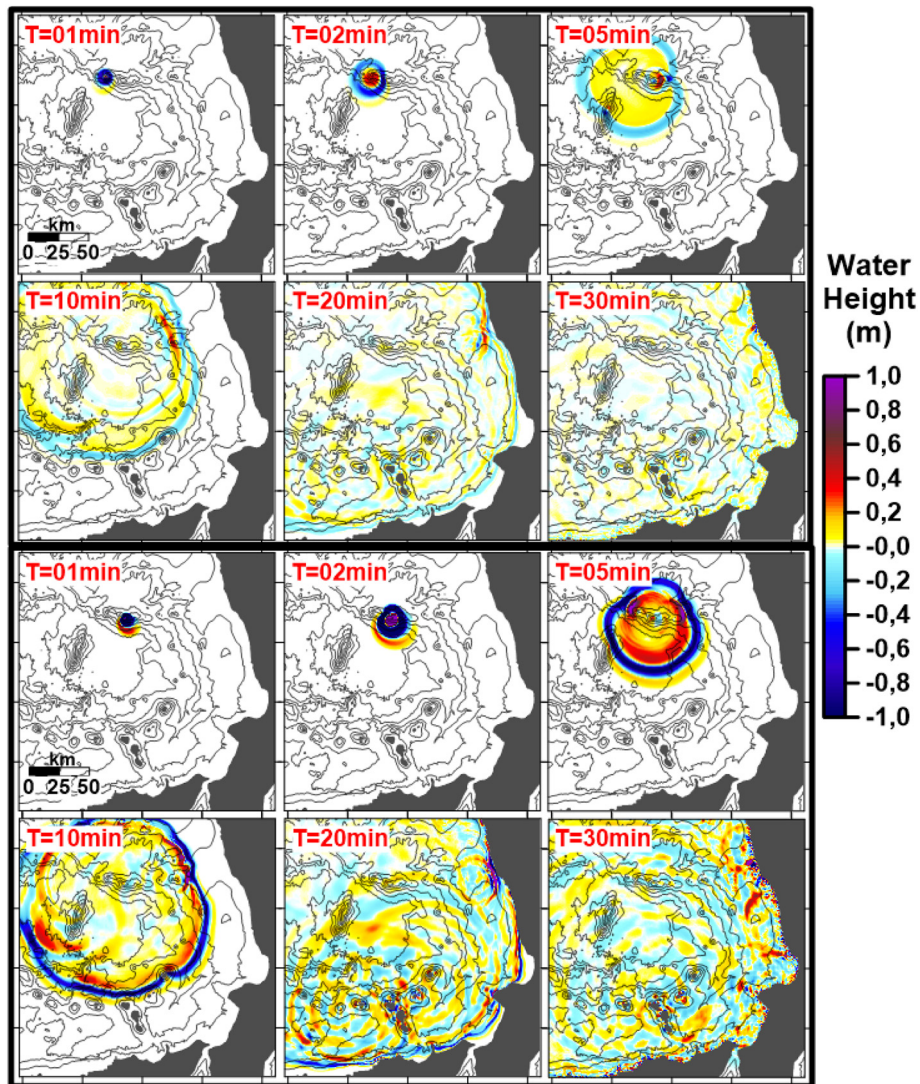
Fig. 8. Sea-elevation fields of the tsunami triggered by the 1.5 km³ (upper 6 panels, case P2) and 2.4 km³ (lower 6 panels, case P3) slides over the south-eastern Tyrrhenian basin.

not generated. In the P2 and P3 cases, the sea surface elevations are in the order of 1 m and 5 m, respectively. We detect the presence of bended paths (beams) where maximum water elevations are found and also cover the PVC summit (Fig. 7). The formation of such beams is due to the interaction of the moving fronts with the seafloor steep-slope morphological alignments (ridges, seamounts, continental margins indentations). The alignment of the Palinuro and Glabro seamounts and the continental margin protrusion offshore northern Calabria act as wave guides to lead the tsunami beam up to the coast. The tsunamis show the highest waves in this coastal stretch, which, as a consequence, represent an area potentially exposed to a relevant hazard. The propagation of the waves for the P2 and P3 scenarios shows similar arrival times (Figs. 8, 9, and 10). The source areas are located at different depths with the P3 slide detaching from the PVC summit at a depth of ~100 m. The P2 initial sliding area is located at a depth ranging from 900 m to 2700 m. This difference contributes to increasing the differences of the two tsunamis, since landslides in deeper waters are known to have less tsunamigenic potential. This effect is included in the UBO-TSUIMP code where changes in the sea floor topography due to the submarine landslide motion are converted to an attenuated sea surface topography with a damping increasing with the local depth of the seabed. The different sizes of the tsunamis are evident from the graphs of water elevation along the coasts (Figs. 9 and 10), where maximum values are found along the Calabrian coast. The Sardinia region results to be less affected

in both cases, due to the larger distance from the sources. Another peculiar aspect is the effect of the Aeolian Islands (Fig. 1), where the waves dissipate and partially protect the Sicilian coasts (Figs. 9 and 10). Our results show that a hazard related to potential tsunamis generated by landslides occur at the PVC. The quantification of this hazard in terms of recurrence times, amount of sliding material, and probability of occurrence is, at the present, not possible on the basis of the available data, but some actions devoted to monitor the seismic activity of the PVC and the stability of the edifice should be embarked. These include networks of ocean bottom sesimometers, bottom pressure gauges located on the PVC and in selected more distal areas, and tide gauges for the detection of abrupt variations in the sea level. In addition, volcanological and geophysical investigations should be carried out to identify 1) those sectors of the PVC affected by hydrothermal activity that can weak the structure of the volcanoes, 2) potentially active scarps related to volcanotectonic, tectonic or gravity instability, and 3) the shallow structure of the PVC flanks characterized by loose deposits. A monitoring of the PVC including the geochemistry of the emitted fluids and periodic campaign oriented to detect variations in the bathymetry could also allow us to detect possible unrest episodes with potentially associated volcano-induced deformations.
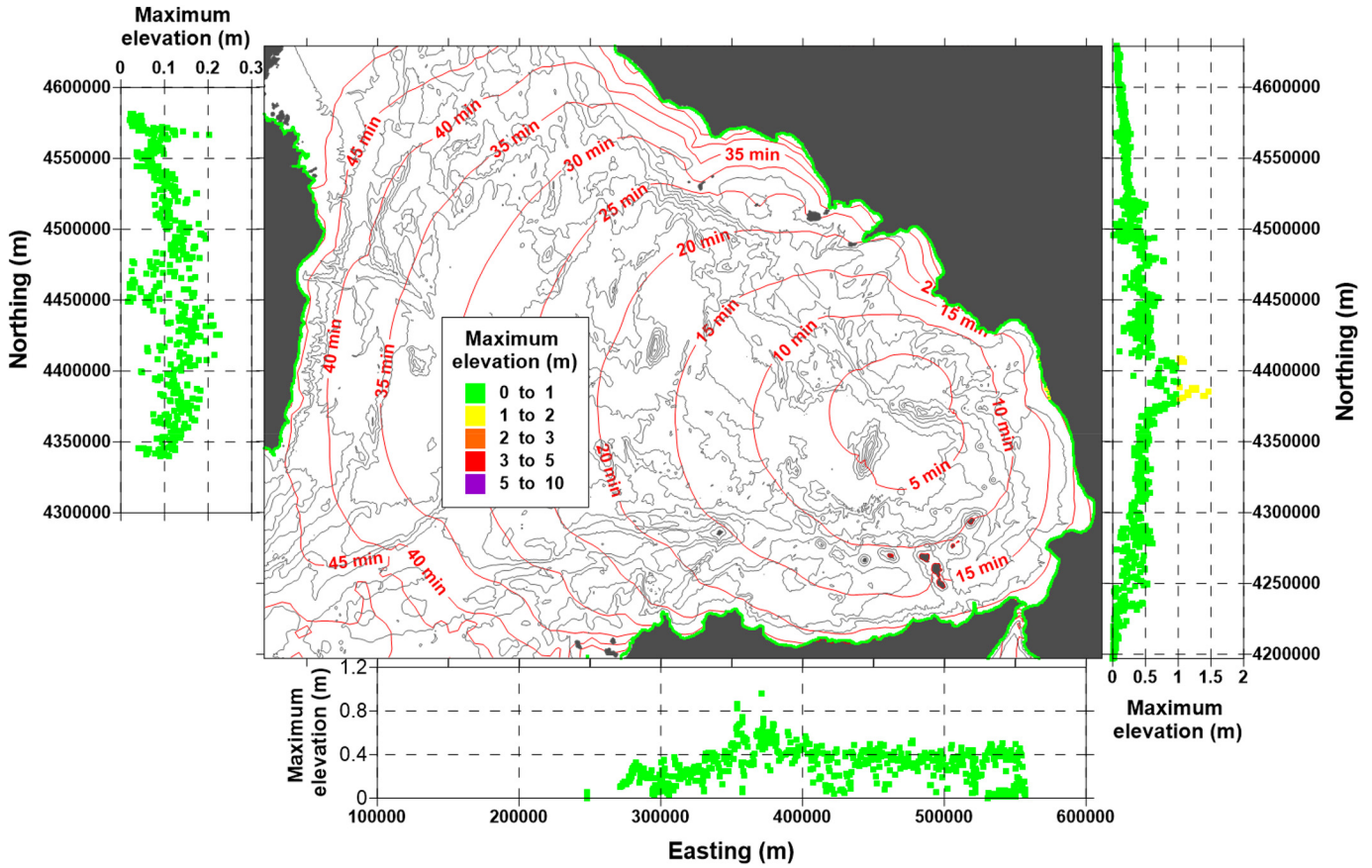
Fig. 9. Scenario P2. The three panels show the maximum water elevation along the 10 m sea depth line for the East Sardinia (left), North Sicily (lower panel), and SE Tyrrhenian (right panel) coasts. Tsunami arrival times are shown every 5 min with red lines. (For interpretation of the references to color in this figure legend, the reader is referred to the web version of this article.)
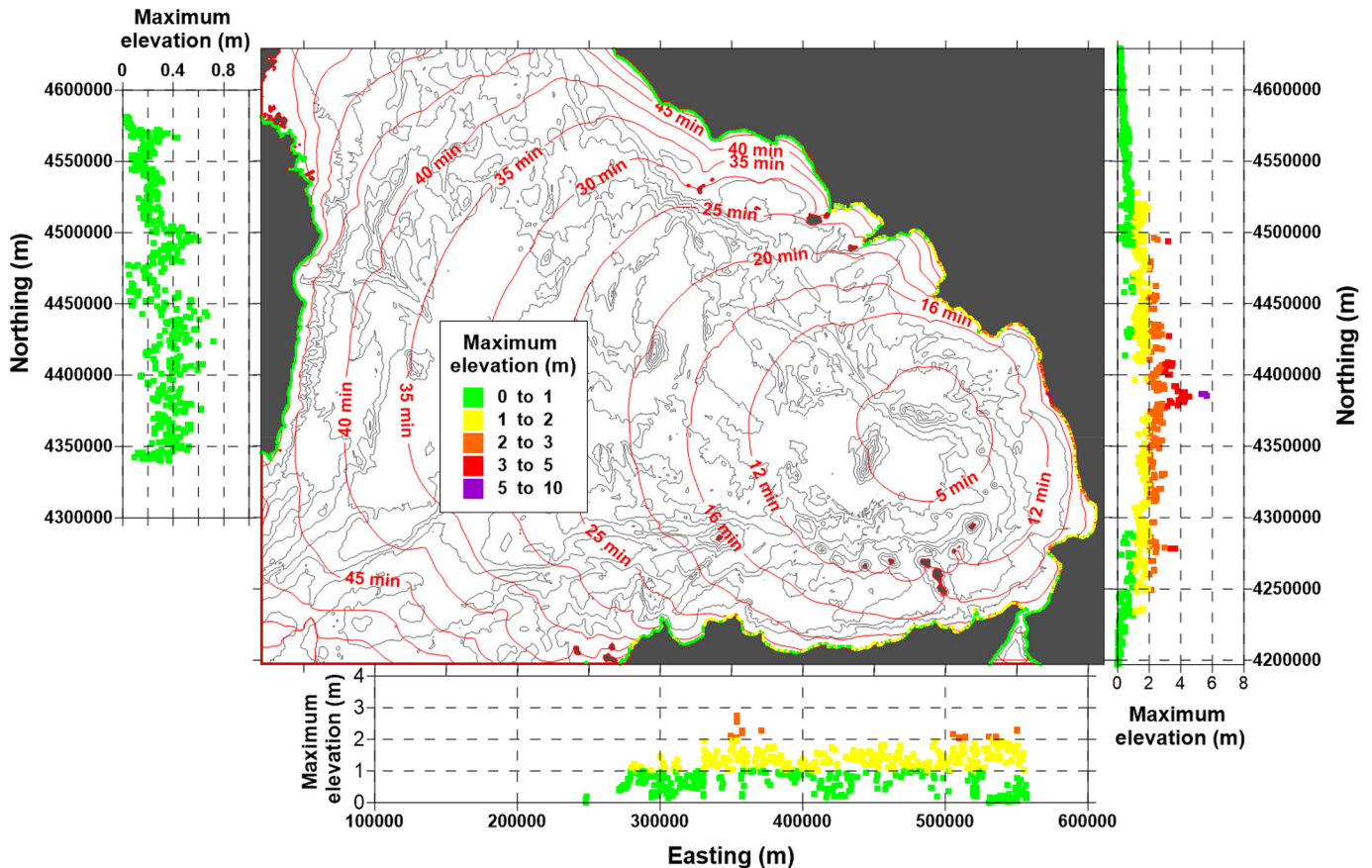

Fig. 10. Scenario P3. See the caption of Fig. 9.

6. Conclusions

We analyze the effects of landslides triggered by possible shallow volcanic earthquakes occurring on the PVC by adopting a scenario-based approach. Our results show that 30% of the tested profiles in the PVC flanks could be destabilized by medium-size shallow earthquakes occurring in their proximity. Landslides reconstructed on the unstable areas result to be tsunamigenic, but only two of the three studied here generate considerable waves. Shapes and propagations are similar, despite the distinct sliding volumes. These results highlight the need for more detailed studies and oceanographic cruises to reveal the nature and characteristics of the PVC and of the other Tyrrhenian seamounts. This information would allow the reconstruction of more exhaustive scenarios to properly assess a landslide-induced tsunami hazard for the Tyrrhenian coasts. Some actions including a multiparametric monitoring network are proposed and should be extended to the other major volcanic complexes of the southern Tyrrhenian Sea including Vavilov, Marsili, and some Aeolian seamounts.

CRediT authorship contribution statement

G. Gallotti: Conceptualization, Methodology, Validation, Investigation, Writing - original draft, Visualization, Writing - review & editing. **S. Passaro:** Formal analysis, Data curation, Visualization. **A. Armigliato:** Methodology, Software, Resources. **F. Zaniboni:** Methodology, Software. **G. Pagnoni:** Methodology, Software, Visualization. **L. Wang:** Methodology, Software, Validation. **M. Sacchi:** Formal analysis, Resources, Data curation. **S. Tinti:** Methodology, Software, Resources, Writing - review & editing, Supervision. **M. Ligi:** Formal analysis, Resources, Data curation, Writing - review & editing, Visualization. **G. Ventura:** Investigation, Writing - original draft, Writing - review & editing, Visualization, Supervision.

Declaration of competing interest

The authors declare that they have no known competing financial interests or personal relationships that could have appeared to influence the work reported in this paper.

Appendix A

Table A1

Computed Factor of Safety F for the investigated profiles (Fig. 2). Values below 1.05 (denoting the transition to instability) are shown in bold. Different PGA and soil parameters have been tested (see Tables 1 and 2). For each profile, the average slope gradient is shown. The most unstable profiles are 1, 7, 11, and 12 under condition s_2.

Profile 1	20°				Profile 8	16°			
PGA	s_1	s_2	s_3	s_4	PGA	s_1	s_2	s_3	s_4
0	1.48	1.44	1.65	1.62	0	2.16	2.34	2.43	2.61
0.05	1.16	1.02	1.30	1.13	0.05	1.58	1.49	1.76	1.67
0.10	**0.92**	**0.74**	1.06	**0.85**	0.10	1.22	1.09	1.08	1.17
0.15	**0.78**	**0.53**	**0.85**	**0.60**	0.15	**1.00**	**0.81**	1.08	**0.91**
Profile 2	15°				**Profile 9**	10°			
PGA	s_1	s_2	s_3	s_4	PGA	s_1	s_2	s_3	s_4
0	2.35	2.56	2.63	2.90	0	3.42	3.70	3.86	4.00
0.05	1.65	1.58	1.86	1.76	0.05	2.21	1.99	2.46	2.25
0.10	1.27	1.13	1.44	1.27	0.10	1.58	1.36	1.81	1.51
0.15	**1.02**	**0.85**	1.16	**0.95**	0.15	1.26	**1.00**	1.41	1.13
Profile 3	10°				**Profile 10**	16°			
PGA	s_1	s_2	s_3	s_4	PGA	s_1	s_2	s_3	s_4
0	3.40	3.82	3.83	4.00	0	2.25	2.61	2.57	2.93
0.05	2.18	2.00	2.42	2.25	0.05	1.69	1.72	1.90	1.94
0.10	1.58	1.34	1.76	1.51	0.10	1.30	1.27	1.50	1.40
0.15	1.23	**0.99**	1.37	1.09	0.15	1.06	**0.95**	1.22	1.10
Profile 4	12°				**Profile 11**	17°			
PGA	s_1	s_2	s_3	s_4	PGA	s_1	s_2	s_3	s_4
0	2.67	2.95	3.02	3.33	0	1.98	1.97	2.21	2.21
0.05	1.83	1.69	2.07	1.90	0.05	1.46	1.30	1.65	1.44
0.10	1.37	1.16	1.55	1.30	0.10	1.13	**0.93**	1.26	1.03
0.15	1.09	**0.89**	1.23	**0.99**	0.15	**0.89**	**0.70**	**1.03**	**0.81**
Profile 5	11°				**Profile 12**	16°			
PGA	s_1	s_2	s_3	s_4	PGA	s_1	s_2	s_3	s_4
0	2.92	3.23	3.30	3.65	0	1.94	1.89	2.21	2.13
0.05	1.97	1.83	2.21	2.07	0.05	1.44	1.26	1.62	1.44
0.10	1.48	1.27	1.65	1.41	0.10	1.13	**0.95**	1.26	1.04
0.15	1.16	**0.95**	1.31	1.06	0.15	**0.91**	**0.72**	**1.04**	**0.82**
Profile 6	10°				**Profile 13**	10°			
PGA	s_1	s_2	s_3	s_4	PGA	s_1	s_2	s_3	s_4
0	3.30	3.37	3.72	3.82	0	4.1	4.6	4.7	5.00
0.05	2.11	1.86	2.39	2.11	0.05	2.61	2.52	2.88	2.89
0.10	1.55	1.27	1.72	1.44	0.10	1.85	1.67	2.12	1.85
0.15	1.20	**0.95**	1.34	1.06	0.15	1.45	1.22	1.62	1.35
Profile 7	15°								
PGA	s_1	s_2	s_3	s_4					
0	2.21	2.25	2.48	2.52					
0.05	1.58	1.41	1.8	1.58					
0.10	1.23	**1.02**	1.35	1.13					
0.15	**0.99**	**0.78**	1.08	**0.86**					

References

Ambraseys, N.N., Simpson, K.A., Bommer, J.J., 1996. Prediction of horizontal response spectra in Europe. Earthq. Eng. Struct. Dyn. 25, 371–400. https://doi.org/10.1002/(SICI)1096-9845(199604)25:4<371::AID-EQE550>3.0.CO;2-A.

Apuani, T., Corazzato, C., 2010. Etna flank dynamics: a sensitivity analysis by numerical modelling. In: Olalla, C., Hernandez, L.E., Rodriguez-Losada, J.A., Gonzalez-Gallego, J. (Eds.), Volcanic Rock Mechanics — Rock Mechanics and Geo-Engineering in Volcanic Environments, Papers from the 3rd ISRM International Workshop, Puerto de la Cruz, Tenerife (Canary Islands), Spain, 31 May–1 June 2010. Taylor & Francis Group, London, pp. 151–157 978-0-415-58478-4.

Beccaluva, L., Gabbianelli, G., Lucchini, F., Rossi, P.L., Savelli, C., 1985. Petrology and K/Ar ages of volcanic dredged from the Eolian seamounts: implications for geodynamic evolution of the Southern Tyrrhenian basin. Earth Planet. Sci. Lett. 74, 187–208.

Bisson, M., Paolillo, A., Tadini, A., Sulpizio, R., Zanchetta, G., 2018. Volcaniclastic flow hazard assessment in highly populated areas: a GIS-based approach applied to Torre del Greco municipality (Somma-Vesuvius, Italy). Geosci. J. 22, 501–522. https://doi.org/10.1007/s12303-017-0060-2.

Caratori Tontini, F., Cocchi, L., Carmisciano, C., 2009. Rapid 3-d forward model of potential fields with application to the Palinuro Seamount magnetic anomaly (southern Tyrrhenian Sea, Italy). J.Geophys. Res.: Solid Earth 114, B02103. https://doi.org/10.1029/2008JB005907.

Caratori Tontini, F., Cocchi, L., Muccini, F., Carmisciano, C., Marani, M., Bonatti, E., Ligi, M., Boschi, E., 2010. Potential-field modeling of collapse-prone submarine volcanoes in the southern Tyrrhenian Sea (Italy). Geophys. Res. Lett. 37. https://doi.org/10.1029/2009GL041757 L03305.

Caratori Tontini, F., Bortoluzzi, G., Carmisciano, C., Cocchi, L., de Ronde, C., Ligi, M., Muccini, F., 2014. Near-bottom magnetic signatures of submarine hydrothermal systems at Marsili and Palinuro Volcanoes, Southern Tyrrhenian Sea, Italy. Econ. Geol. 109, 2119–2128.

CEN (ComitèEuropèen de Normalisation), 2003. prEN 1998–1-Eurocode 8: Design of Structures for Earthquake Resistance. Part 1: General Rules, Seismic Actions and Rules for Buildings. Draft no 6, Doc CEN/TC250/SC8/N335, January 2003 (Brussels).

Cocchi, L., Passaro, S., Caratori Tontini, F., Ventura, G., 2017. Volcanism in slab tear faults is larger than in island-arcs and back-arcs. NatureCommun 8, 1451. https://doi.org/10.1038/s41467-017-01626-w.

Colantoni, P., Lucchini, F., Rossi, P.L., Sartori, R., Savelli, C., 1981. The Palinuro volcano and magmatism of the southeastern Tyrrhenian Sea (Mediterranean). Mar. Geol. 39, M1–M12.

D'Alessandro, A., D'Anna, G., Luzio, D., Mangano, G., 2009. The INGV's new OBS/H: analysis of the signals recorded at the Marsili submarine volcano. J. Volcanol. Geotherm. Res. 183, 17–29.

Dekov, V.M., Savelli, C., 2004. Hydrothermal activity in the SE Tyrrhenian Sea: an overview of 30 years of research. Mar. Geol. 204, 161–185.

Del Ben, A., Barnaba, C., Taboga, A., 2008. Strike-slip systems as the main tectonic features in the Plio-Quaternary kinematics of the Calabrian Arc. Mar. Geophys. Res. 29, 1–12.

del Potro, R., Hürlimann, M., 2008. Geotechnical classification and characterisation of materials for stability analyses of large volcanic slopes. Eng. Geol. 98, 1–17.

Doglioni, C., Ligi, M., Scrocca, D., Bigi, S., Bortoluzzi, G., Carminati, E., Cuffaro, M., D'Oriano, F., Forleo, V., Muccini, F., Riguzzi, F., 2012. The tectonic puzzle of the Messina area (Southern Italy): insights from new seismic reflection data. Sci. Rep. 2. https://doi.org/10.1038/srep00970.

Dondin, F.J.-Y., Heap, M.J., Robertson, R.E.A., Dorville, J.-F.M., Carey, S., 2016. Flank instability assessment at Kick-'em-Jenny submarine volcano (Grenada, Lesser Antilles): a multidisciplinary approach using experiments and modeling. Bull. Volcanol. 79, 5. https://doi.org/10.1007/s00445-016-1090-8.

EMODnet Bathymetry Consortium, 2018. EMODnet Digital Bathymetry (DTM). http://doi.org/10.12770/18ff0d48-b203-4a65-94a9-5fd8b0ec35f6.

Enet, F., Grilli, S.T., 2007. Experimental study of tsunami generation by three dimensional rigid underwater landslides. J. Waterw. Port Coast. Ocean Eng. 133, 442–454.

Faccenna, C., Funiciello, F., Civetta, L., D Antonio, M., Moroni, M., Piromallo, C., 2007. Slab disruption, mantle circulation, and the opening of the Tyrrhenian basins. In: Beccaluva, L., Bianchini, G., Wilson, M. (Eds.), Cenozoic Volcanism in the Mediterranean Area. Geol. Soc. America Special Paper vol. 418, pp. 153–169. https://doi.org/10.1130/2007.2418(08).

Guarnieri, P., 2006. Plio-Quaternary segmentation of the south Tyrrhenian forearc basin. Int. J. Earth Sci. (Geol. Rundsch.) 95, 107–118.

Harbitz, C.B., Løvholt, F., Pedersen, G., Masson, D.G., 2006. Mechanisms of tsunami generation by submarine landslides: a short review. Nor. J. Geol. 86, 255–264.

Harnett, C.E., Kendrick, J.E., Lamur, A., Thomas, M.E., Stinton, A., Wallace, P.A., Utley, J.E.P., Murphy, W., Neuberg, J., Lavallée, Y., 2019. Evolution of mechanical properties of lava dome rocks across the 1995–2010 eruption of Soufrière Hills Volcano, Montserrat. Front. Earth Sci. 7, 7. https://doi.org/10.3389/feart.2019.00007.

Innangi, S., Passaro, S., Tonielli, R., Ventura, G., Tamburrino, S., 2016. Seafloor mapping by using high-resolution multibeam backscatter: a case study from the Palinuro Seamount (Eastern Tyrrhenian Sea). J. Map 12, 736–746.

Janbu, N., 1973. Soil stability computations. In: Hirschfeld, R.C., Poulos, S.J. (Eds.), Embankment-Dam Engineering. Casagrande, John Wiley & Sons, New York, pp. 47–83.

Kalatehjari, R., Ali, N., 2013. A review of three-dimensional slope stability analyses based on limit equilibrium method. Electron. J. Geotech. Eng. 18, 119–134.

Kelfoun, K., Giachetti, T., Labazuy, P., 2010. Landslide-generated tsunamis at Réunion Island. J.Geophys.Res. 115, F04012. https://doi.org/10.1029/2009JF001381.

Kirby, J.T., Shi, F., Nicolsky, D., Misra, S., 2016. The 27 April 1975 Kitimat, British Columbia, submarine landslide tsunami: a comparison of modelling approaches. Landslides 13, 1421–1434. https://doi.org/10.1007/s10346-016-0682-x.

Kowalik, Z., Knight, W., Logan, T., Whitmore, P., 2007. The tsunami of 26 December 2004: numerical modeling and energy considerations. Pure Appl. Geophys. 164, 379–393.

Lanzano, G., Luzi, L., 2020. A ground motion model for volcanic areas in Italy. Bull. Earthq. Eng. 8, 57–76. https://doi.org/10.1007/s10518-019-00735-9.

Ligi, M., Cocchi, L., Bortoluzzi, G., D'Oriano, F., Muccini, F., Tontini, F.C., De Ronde, C.E.J., Carmisciano, C., 2014. Mapping of seafloor hydrothermally altered rocks using geophysical methods: Marsili and Palinuro seamounts, southern Tyrrhenian Sea. Econ. Geol. 109, 2103–2117.

Løvholt, F., Pedersen, G., Harbitz, C.B., Glimsdal, S., Kim, J., 2015. On the characteristics of landslide tsunamis. Phil. Trans. R. Soc. A 373, 20140376. https://doi.org/10.1098/rsta.2014.0376.

Lupton, J., De Ronde, C., Sprovieri, M., Baker, E.T., Bruno, P.P., Italiano, F., Walker, S., Faure, K., Leybourne, M., Britten, K., Greene, R., 2011. Active hydrothermal discharge on the submarine Aeolian Arc. J. Geophys. Res. Solid Earth 116, B02102. https://doi.org/10.1029/2010JB007738.

Malagnini, L., Scognamiglio, L., Mercuri, A., Akinci, A., Mayeda, K., 2008. Strong evidence for non-similar earthquake source scaling in central Italy. Geophys. Res. Lett. 35, L17303. https://doi.org/10.1029/2008GL034310.

Malinverno, A., Ryan, W.B.F., 1986. Extension in the Tyrrhenian Sea and shortening in the Apennines as result of arc migration driven by sinking of the lithosphere. Tectonics 5, 227–245. https://doi.org/10.1029/TC005i002p00227.

Maramai, A., Graziani, L., Alessio, G., Burrato, P., Colini, L., Cucci, L., Nappi, R., Nardi, A., Vilardo, G., 2005. Near- and far-field survey report of the 30 December 2002 Stromboli Southern Italy tsunami. Mar. Geol. 215, 93–106. https://doi.org/10.1016/j.margeo.2004.11.009.

McGuire, W.J., 1996. Volcano Instability: A Review of Contemporary Themes. vol. 110. Geological Society, London, Special Publications, pp. 1–23 1 January 1996. https://doi.org/10.1144/GSL.SP.1996.110.01.01.

McNutt, S.R., Roman, D.C., 2015. Volcanic Seismicity - The Encyclopaedia of Volcanoes (Second Edition). , pp. 1011–1034 https://doi.org/10.1016/B978-0-12-385938-9.00059-6.

McPhie, J., 1995. A Pliocene shoaling basaltic seamount: Ba volcanic group at Rakiraki, Fiji. J. Volcanol. Geotherm. Res. 64, 193–210.

Milano, G., Passaro, S., Sprovieri, M., 2012. Present-day knowledge on the Palinuro Seamount (Southeastern Tyrrhenian Sea). Boll. Geofis. Teor. Appl. 53, 403–416.

Muhari, A., Heidarzadeh, M., Nugroho, H.D., Kriswati, E., Supartoyo, Wijanarto, A.B., Afriyanto, B., Imamura, F., Arikawa, T., 2019. The December 2018 Anak Krakatau volcano tsunami as inferred from post-tsunami field surveys and spectral analysis. Pure Appl. Geophys. 176, 5219–5233. https://doi.org/10.1007/s00024-019-02358-2.

Okal, E.A., Synolakis, C.E., 2004. Source discriminants for nearfield tsunamis. Geophys. J. Int. 158, 899–912. https://doi.org/10.1111/j.1365-246X.2004.02347.x.

Papparo, M.A., Tinti, S., 2017. Analysis of seismic-driven instability of Mt. Nuovo in the Ischia Island, Italy. Bull. of the Seismological Soc. of America 107, 750–759.

Paris, R., 2015. Source mechanisms of volcanic tsunamis. Phil. Trans. R. Soc. A 373, 20140380. https://doi.org/10.1098/rsta.2014.0380.

Passaro, S., Milano, G., D'Isanto, C., Ruggieri, S., Tonielli, R., Bruno, P.P., Sprovieri, M., Marsella, E., 2010. DTM-based morphometry of the Palinuro seamount (Eastern Tyrrhenian Sea): geomorphological and volcanological implications. Geomorphology 115, 129–140. https://doi.org/10.1016/j.geomorph.2009.09.041.

Passaro, S., Ferranti, L., de Alteriis, G., 2011a. The use of high resolution elevation histograms for mapping submerged terraces: a test from the Eastern Tyrrhenian Sea and the Eastern Atlantic Ocean. Quat. Int. 232, 238–249.

Passaro, S., Milano, G., Sprovieri, M., Ruggieri, S., Marsella, E., 2011b. Quaternary still-stand landforms and relations with flank instability events of the Palinuro Bank (southeastern Tyrrhenian Sea). Quat. Int. 232, 228–237.

Pensa, A., Pinton, A., Vita, L., Bonamico, A., De Benedetti, A.A., Giordano, G., 2019. ATLAS of Italian submarine volcanic structures. Memorie Descrittive della Carta Geologica d'Italia 104, 77–183.

Putra, P.S., Aswan, A., Maryunani, K.A., Yulianto, E., Nugroho, S.H., Setiawan, V., 2020. Postevent field survey of the 22 December 2018 Anak Krakatau Tsunami. Pure Appl. Geophys. https://doi.org/10.1007/s00024-020-02446-8.

Rabinovich, A.B., Titov, V.V., Moore, C.W., Eble, M.C., 2017. The 2004 Sumatra Tsunami in the Southeastern Pacific Ocean: new global insight from observations and modeling. J. Geophys. Res.: Oceans 122, 7992–8019. https://doi.org/10.1002/2017JC013078.

Reid, M.E., Sisson, T.W., Brien, D.L., 2001. Volcano collapse promoted by hydrothermal alteration and edifice shape, Mount Rainer, Washington. Geology 79, 779–782.

Rovida, A., Locati, M., Camassi, R., Lolli, B., Gasperini, P., 2019. Catalogo Parametrico dei Terremoti Italiani (CPTI15), versione 2.0. Istituto Nazionale di Geofisica e Vulcanologia (INGV) https://doi.org/10.13127/CPTI/CPTI15.2.

Sabetta, F., Pugliese, A., 1987. Attenuation of peak horizontal acceleration and velocity from Italian strongmotion records. Bull. Seismol. Soc. Am. 77, 1491–1513.

Safipour, R., Hölz, S., Halbach, J., Jegen, M., Petersen, S., Swidinsky, A., 2017. A self-potential investigation of submarine massive sulfides: Palinuro Seamount, Tyrrhenian Sea. Geophysics 82, A51–A56.

Sarma, S.K., 1979. Stability analysis of embankments and slopes. J. Geotech. Eng. Div. ASCE 105, 1511–1524.

Savage, S.B., Hutter, K., 1989. The motion of a finite mass of granular material down a rough incline. Fluid. Mech. 199, 177–215.

Schaefer, L.N., Oommen, T., Corazzato, C., Tibaldi, A., Escobar-Wolf, R.I., Rose, W., 2013. An integrated field-numerical approach to assess slope stability hazards at volcanoes: the example of Pacaya, Guatemala. Bull. Volcanol. 75, 720. https://doi.org/10.1007/s00445-013-0720-7.

Schaefer, L.N., Kendrick, J.E., Oommen, T., Lavallée, Y., Chigna, G., 2015. Geomechanical rock properties of a basaltic volcano. Front. Earth Sci. 3, 29. https://doi.org/10.3389/feart.2015.00029.

Schiffman, P., Watters, R.J., Thompson, N., Walton, A.W., 2006. Hyaloclastites and the slope stability of Hawaiian volcanoes: insights from the Hawaiian Scientific Drilling Project's 3-km drill core. J. Volcanol. Geotherm. Res. 151, 217–228. https://doi.org/10.1016/j.jvolgeores.2005.07.030.

Seisdedos, J., Ferrer, M., González de Vallejo, L.I., 2012. Geological and geomechanical models of the pre-landslide volcanic edifice of Güímar and La Orotava megalandslides (Tenerife). J. Volcanol. Geotherm. Res. 239-240, 92–110.

Soloviev, S.L., Kuzin, I.P., Kovachev, S.A., Ferri, M., Guerra, I., Luongo, G., 1990. Microearthquakes in the Tyrrhenian Sea as revealed by joint land and sea-bottom seismographs. Mar. Geol. 94, 131–146.

Szitkar, F., Petersen, S., Caratori Tontini, F., Cocchi, L., 2015. High-resolution magnetics reveal the deep structure of a volcanic-arc-related basalt-hosted hydrothermal site

(Palinuro, Tyrrhenian Sea). Geochem. Geophys. Geosyst. 16, 1950–1961. https://doi.org/10.1002/2015GC005769.

Thouret, J.C., 1999. Volcanic geomorphology—an overview. Earth-Sci. Rev. 47, 95–131.

Thouret, J.C., 2010. Volcanic hazards and risks: a geomorphological perspective. In: Goudie, e.I.A.-A.a.A.S. (Ed.), Geomorphological Hazards and Disaster Prevention. Cambridge University Press, pp. 13–32.

Tinti, S., Manucci, A., 2006. Gravitational stability computed through the limit equilibrium method revisited. Geophys. J. Int. 164, 1–14.

Tinti, S., Manucci, A., 2008. A new computational method based on the minimum lithostatic deviation (MLD) principle to analyse slope stability in the frame of the 2-D limit-equilibrium theory. Nat. Hazards Earth Syst. Sci. 8, 671–683.

Tinti, S., Tonini, R., 2013. The UBO-TSUFD tsunami inundation model: validation and application to a tsunami case study focused on the city of Catania, Italy. Nat. Hazards Earth Syst. Sci. 13, 1795–1816. https://doi.org/10.5194/nhess-13-1795-2013.

Tinti, S., Bortolucci, E., Vannini, C., 1997. A block-based theoretical model suited to gravitational sliding. Nat. Hazards 16, 1–28.

Tinti, S., Chiocci, F.L., Zaniboni, F., Pagnoni, G., de Alteriis, G., 2011. Numerical simulation of the tsunami generated by a past catastrophic landslide on the volcanic island of Ischia, Italy. Mar. Geophys. Res. 32, 287–297. https://doi.org/10.1007/s11001-010-9109-6.

Titov, V.V., Rabinovich, A.B., Mofjeld, H., Thomson, R.E., Gonzalez, F.I., 2005. The global reach of the 26 December 2004 Sumatra tsunami. Science 309, 2045–2048.

Tusa, G., Langer, H., 2016. Prediction of ground motion parameters for the volcanic area of Mount Etna. J. Seismol. 20, 1–42. https://doi.org/10.1007/s10950-015-9508-x.

Ulvrová, M., Paris, R., Nomikou, P., Kelfoun, K., Leibrandt, S., Tappin, D., McCoy, F., 2016. Source of the tsunami generated by the 1650 AD eruption of Kolumbo submarine volcano (Aegean Sea, Greece). J. Volcanol. Geotherm. Res. 321, 125–139.

van Wyk de Vries, B., Delcamp, A., 2016. Volcanicdebris avalanches. In: Davies, T. (Ed.), Landslide hazards, risks, and disasters. Elsevier, Amsterdam, pp. 131–153.

van Wyk de Vries, B., Francis, P., 1997. Catastrophic collapse at stratovolcanoes induced by gradual volcano spreading. Nature 387, 387–390.

Voight, B., Elsworth, D., 1997. Failure of volcano slopes. Geotechnique 47, 1–31.

Wang, L., Zaniboni, F., Tinti, S., Zhang, X., 2019. Reconstruction of the 1783 Scilla landslide, Italy: numerical investigations on the flow-like behaviour of landslides. Landslides 16, 1065–1076.

Ward, S.N., Day, S., 2001. Cumbre Vieja Volcano - Potential collapse and tsunami at La Palma, Canary Islands. Geophys. Res. Lett. 28, 3397–3400.

Xia, X., Liang, Q., 2018. A new depth-averaged model for flow-like landslides over complex terrains with curvatures and steep slopes. Eng. Geol. 234, 174–191.

Yavari-Ramshe, S., Ataie-Ashtiani, I.B., 2016. Numerical modeling of subaerial and submarine landslide-generated tsunami waves-recent advances and future challenges. Landslides 13, 1325–1368. https://doi.org/10.1007/s10346-016-0734-2.

Zaniboni, F., Tinti, S., 2019. The 1963 Vajont landslide: a numerical investigation on the sliding surface heterogeneity. Pure Appl. Geophys. 176, 279–295. https://doi.org/10.1007/s00024-018-2023-6.

Zaniboni, F., Pagnoni, G., Tinti, S., Della Seta, M., Fredi, P., Marotta, E., Orsi, G., 2013. The potential failure of Monte Nuovo at Ischia Island (Southern Italy): numerical assessment of a likely induced tsunami and its effects on a densely inhabited area. Bull. Volcanol. 75, 763. https://doi.org/10.1007/s00445-013-0763-9.

Zaniboni, F., Armigliato, A., Pagnoni, G., Tinti, S., 2014. Continental margins as a source of tsunami hazard: the 1977 Gioia Tauro (Italy) landslide-tsunami investigated through numerical modelling. Mar. Geol. 357, 210–217.